

# Normal contact with high order finite elements and a fictitious contact material

Tino Bog<sup>a,\*</sup>, Nils Zander<sup>a</sup>, Stefan Kollmannsberger<sup>a</sup>, Ernst Rank<sup>a</sup>

<sup>a</sup>*Chair for Computation in Engineering, Faculty of Civil, Geo and Environmental Engineering, Technische Universität München, Arcisstrasse 21, 80333 München, Germany*

---

## Abstract

Contact problems in solid mechanics are traditionally solved using the  $h$ -version of the finite element method. The constraints are enforced along the surfaces of e.g. elastic bodies under consideration. Standard constraint algorithms include penalty methods, Lagrange multiplier methods and combinations thereof. For complex scenarios, a major part of the solution time is taken up by operations to identify points that come into contact. This paper presents a novel approach to model frictionless contact using high order finite elements. Here, we employ an especially designed material model that is inserted into two- respectively three-dimensional regions surrounding contacting bodies. Contact constraints are thus enforced on the same manifold as the accompanying structural problem. The application of the current material formulation leads to a regularization of the Karush-Kuhn-Tucker conditions. Our formulation can be classified as a barrier-type method. Results are obtained for two- and three-dimensional problems, including a Hertzian contact problem. Comparisons to a commercial FEA package are provided. The proposed formulation works well for non-matching discretizations on adjacent contact interfaces and handles self-contact naturally. Since the non-penetrating conditions are solved in a physically consistent manner, there is no need for an explicit contact search.

*Keywords:* high order finite elements,  $p$ -fem, contact mechanics, domain contact, frictionless contact, finite cell method, Hertzian contact

---

## 1. Introduction

The simulation of mechanical contact phenomena is of interest in various fields of engineering. Mechanical systems usually consist of several parts, and their interaction needs to be represented correctly.

---

\*Corresponding author

*Email addresses:* [tino.bog@tum.de](mailto:tino.bog@tum.de) (Tino Bog), [nils.zander@tum.de](mailto:nils.zander@tum.de) (Nils Zander), [stefan.kollmannsberger@tum.de](mailto:stefan.kollmannsberger@tum.de) (Stefan Kollmannsberger), [ernst.rank@tum.de](mailto:ernst.rank@tum.de) (Ernst Rank)

Numerical solutions for contact problems are mostly obtained by applying the finite element method (FEM) [1, 2]. The overwhelming part of the literature is concerned with the classical  $h$ -version of the FEM, which uses linear or at most quadratic ansatz functions for spatial discretization. Contact constraints are enforced along contact interfaces defined on the surfaces of e.g. elastic bodies under consideration. Early discretizations of these interfaces were based on so-called *node-to-node* contact elements, for which the nodal positions of adjacent bodies had to match at the interface [3–5]. Because of the limited applicability of this approach, e.g. *node-to-segment* contact elements were developed allowing the nodes to slide along the whole contact interface [6, 7]. However, non-smooth surfaces, which typically arise in linear FE meshes for the  $h$ -version, pose a challenge for this kind of formulation. For problems involving large sliding, nodes can get stuck at re-entrant corners. To overcome this issue, mortar-type methods have been developed, which enforce contact constraints in a weak (integral) sense [8–15].

Recently, high order discretizations have been introduced to the realm of contact mechanics. These discretizations offer advantages concerning the overall accuracy of the numerical approximation as well as a smoother and, thus, improved description of the contact interface. The contributions made cover the  $p$ -version of the finite element method [16–18] and NURBS basis functions used in isogeometric analysis (IGA) [19, 20].

Different possibilities have been developed for the enforcement of contact constraints. The predominant approaches are the penalty method, the Lagrange multiplier method and combinations thereof [21, 22]. Furthermore, barrier methods [23], Nitsche’s method [24, 25] and the formulation of Dirichlet-Neumann problems [26] have been applied successfully.

Since contact constraints are generally of inequality type, even problems of linear elasticity are rendered non-linear. Hence, these problems are generally solved iteratively [21]. Here, each iteration is characterized by a global search for bodies likely to come into contact, a local search at element level for changes in the state of contact such as penetration or stick/slip, and the actual enforcement of contact constraints. For complex contact scenarios, the search for contact can make up a major part of a simulation [1].

In recent years, formulations have been introduced, which utilize alternative discretizations for the contact interface or employ new schemes to enforce contact constraints. Oñate et al. proposed an approach for contact modeling in the context of the *particle element method* [27]. Here, nodes are regarded as particles carrying all relevant solution information. In every time step, a new mesh is created from the positions of the particles using a Delaunay triangulation to solve the elasticity problem by means of linear finite elements. When the mesh is created, contact elements are identified as simplices that connect different bodies or are attached to a rigid surface. Inside these contact elements, internal forces are applied to avoid normal penetration and to model friction.

Another approach, introduced by Oliver and co-workers, is the *contact domain method* [28, 29]. Their idea is to introduce a contact mesh of linear triangles—the contact domain—between bodies in close proximity. This contact

mesh is then used to establish normal and tangential gap measures. Contact constraints are enforced using Lagrange multipliers.

A formulation similar to the one followed in the publication at hand, yet using the  $h$ -version of the FEM, was introduced as the *third medium approach* by Wriggers et al. [30]. Here, the authors embed elastic bodies in a special contact material. This material consists of a highly compliant isotropic part and an anisotropic part. The latter is activated once the contact material is compressed below a certain threshold.

In this paper, we propose an approach that combines a material formulation to enforce contact constraints and a high order discretization, namely the  $p$ -version of the finite element method. Our contribution is motivated by the *finite cell method* (FCM), an embedded domain method based on high order finite elements [31, 32]. Alike FCM, this contact formulation embeds the original domain of computation in a larger 'fictitious' domain, yet here not considered as 'void' material but as a non-linear medium to avoid penetration of surfaces. The application of a contact material enforces contact constraints in a physically consistent manner by relying on the growth condition [33] and can, thus, be classified as a barrier type method [21]. Also, there is no need for an explicit contact search, since the contact status is based on the deformation of the contact material. In contrast to the work by Wriggers et al. [30], our formulation only demands for a single material parameter and employs a consistent linearization. Furthermore, by using the  $p$ -version of the FEM, complex deformation scenarios can be recovered using only few coarse elements. As this approach can readily be combined with the finite cell method, it simplifies mesh generation significantly, as e.g. voids or fillets in the structure need not be explicitly represented by element boundaries.

The present work is outlined as follows: Section 2 recalls the basic features of the  $p$ -version of the finite element method and the finite cell method. Section 3 introduces a formulation for the enforcement of contact constraints using a contact material. The new approach will be illustrated by numerical examples in Section 4. The paper closes with some concluding remarks in Section 5.

## 2. High order finite elements and the finite cell method

The current section gives a short overview of the  $p$ -version of the finite element method as well as the finite cell method (FCM). The latter is fundamental to the contact approach outlined in this publication and is used in some of the examples presented in Section 4 for modelling small geometric features such as voids or fillets. Here, the overview is limited to the extent necessary to understand the rest of the paper. For further details on  $p$ -FEM and FCM the reader is referred to [31, 32, 34, 35].

### 2.1. High order finite elements ( $p$ -FEM)

The calculations in this publication have been performed using the  $p$ -version of the finite element method. The main benefits of the  $p$ -version are exponential convergence for smooth problems, insensitivity to mesh distortion and

well-behaved condition numbers for increasing polynomial orders. Just like conventional finite elements, the  $p$ -version of the FEM is based on a weak form of the partial differential equation under consideration. Fitting the scope of the paper at hand, this shall be exemplified for the case of hyperelasticity by applying the principle of virtual work

$$\delta\mathcal{W}(\mathbf{u}, \delta\mathbf{u}) = \int_{\Omega} \boldsymbol{\sigma} : \delta\boldsymbol{\epsilon} dv - \int_{\Omega} \mathbf{f} \cdot \delta\mathbf{u} dv - \int_{\Gamma_N} \mathbf{t} \cdot \delta\mathbf{u} ds = 0 \quad (1)$$

Here,  $\boldsymbol{\sigma}$  and  $\delta\boldsymbol{\epsilon}$  are the Cauchy stress tensor and the variation of the Euler-Almansi strain tensor, respectively, while  $\mathbf{f}$  denotes a body load defined in a physical domain  $\Omega$ . The prescribed surface tractions  $\mathbf{t}$  are defined on the Neumann boundary  $\Gamma_N$  [36, 37]. The displacement solution  $\mathbf{u}$  and its variation  $\delta\mathbf{u}$  are taken from appropriate Sobolev spaces, with  $\mathbf{u}$  fulfilling Dirichlet boundary conditions. Both  $\mathbf{u}$  and  $\delta\mathbf{u}$  are discretized to yield an approximate solution using a linear combination of ansatz functions  $\{N_1, N_2, \dots, N_n\}$ :

$$\mathbf{u}_h = \sum_{i=1}^n \mathbf{N}_i \tilde{\mathbf{u}}_i, \quad (2)$$

where  $\tilde{\mathbf{u}}_i$  denotes the degrees of freedom (DOF) related to the ansatz function  $N_i$ . The same ansatz functions  $\mathbf{N}_i$  are also used to approximate the variation of the solution  $\delta\mathbf{u}$  [38]. In the one-dimensional case, the ansatz functions of the  $p$ -version are constructed as follows

$$N_1^{1D}(\xi) = \frac{1}{2} (1 - \xi) \quad (3)$$

$$N_2^{1D}(\xi) = \frac{1}{2} (1 + \xi) \quad (4)$$

$$N_i^{1D}(\xi) = \phi_{i-1}(\xi), \quad i = 3, \dots, p+1, \quad (5)$$

where the first two modes are the linear shape functions known from the  $h$ -version and  $\phi_i$  are integrated Legendre polynomials [35] defined as

$$\phi_j(\xi) = \sqrt{\frac{2j-1}{2}} \int_1^\xi P_{j-1}(x) dx \quad (6)$$

$$= \frac{1}{\sqrt{(4j-2)}} (P_j(\xi) - P_{j-2}(\xi)), \quad j = 2, 3, \dots \quad (7)$$

The two- and three-dimensional ansatz spaces are constructed as tensor products of the one-dimensional basis:

$$\mathbf{N}^{2D}(\xi, \eta) = \mathbf{N}^{1D}(\xi) \otimes \mathbf{N}^{1D}(\eta) \quad (8)$$

$$\mathbf{N}^{3D}(\xi, \eta, \zeta) = \mathbf{N}^{1D}(\xi) \otimes \mathbf{N}^{1D}(\eta) \otimes \mathbf{N}^{1D}(\zeta). \quad (9)$$

There are also modifications of these ansatz spaces, such as the trunk and anisotropic tensor space [39, 40], to improve the numerical efficiency for certain problem classes.

## 2.2. Finite cell method (FCM)

One of the basic challenges of applying finite elements is to create a spatial discretization (mesh). Mesh generation tends to become laborious—especially for complex geometries. To overcome this issue, fictitious domain methods have been developed, which do not need a conforming discretization of the problem geometry. One such fictitious domain approach is the finite cell method (FCM), which utilizes high order finite elements [31, 32]. As such it embeds physical bodies of arbitrary shape into a simple Cartesian domain, which can be discretized in a straightforward manner by means of structured grids. The geometry of the physical bodies is recovered on the integration level using an indicator function  $\alpha(\mathbf{X})$ , which is evaluated at a material point  $\mathbf{X}$ . It has been shown in many examples, that the FCM delivers accurate results even for non-smooth problems. So far integrated Legendre polynomials ( $p$ -FEM) [31, 32], NURBS (IGA) [41, 42] and Lagrange polynomials (Spectral Cell Method) [43, 44] have been applied successfully. Dauge et al. [45] showed that for smooth problems the  $p$ -extension of the ansatz space even yields exponential rates of convergence for the FCM. A thorough overview of the finite cell method can be found in the recent review article by Schillinger and Ruess [46].

Until this point, our statements served to sum up the basics of the  $p$ -version of the FEM, which determines the scheme of our formulation. Now, the FCM-based idea of filling void regions with a fictitious, highly compliant material will be adopted for the contact formulation at hand. But other than simplifying mesh generation for complex geometries, we will circumvent the explicit contact search by filling gaps with a stiffening contact material. The respective material formulation will be introduced in the following section.

## 3. Contact material formulation

The contact material used in our approach (similar to the one recently introduced by Wriggers et al. [30]) resembles the fictitious material used by the FCM (see Section 2.2) until contact surfaces come in close proximity. It is only in this limit case that the contact material undergoes a substantial stiffening and generates the internal forces necessary to enforce the normal contact constraints. Note however, that all possible contact interfaces (and only these!) are assumed to be discretized conformingly by element boundaries. This differs from the general FCM-concept, where all domain boundaries may pass through the interior of elements. A non-conforming transition from physical to contact material within one element would cause significant oscillation in the approximate solution and a reduction of accuracy.

### 3.1. Governing equations

The deformations  $\mathbf{u}_{phys}$  and  $\mathbf{u}_{cont}$  of the physical and contact domain, respectively, are governed by the following partial differential equations:

$$\nabla \cdot \boldsymbol{\sigma}_{phys} + \mathbf{f} = \mathbf{0} \quad \text{in } \Omega_{phys} \quad (10)$$

$$\mathbf{u}_{phys} = \bar{\mathbf{u}} \quad \text{on } \Gamma_D \quad (11)$$

$$\boldsymbol{\sigma}_{phys} \cdot \mathbf{n} = \mathbf{t} \quad \text{on } \Gamma_{N,phys} \quad (12)$$

$$\nabla \cdot \boldsymbol{\sigma}_{cont} = \mathbf{0} \quad \text{in } \Omega_{cont} \quad (13)$$

$$\mathbf{u}_{phys} = \mathbf{u}_{cont} \quad \text{on } \Gamma_I \quad (14)$$

$$\boldsymbol{\sigma}_{cont} \cdot \mathbf{n} = \mathbf{0} \quad \text{on } \Gamma_{N,cont}, \quad (15)$$

where  $\boldsymbol{\sigma}_{phys}$  and  $\boldsymbol{\sigma}_{cont}$  are the Cauchy stress tensors in the physical and contact domain, respectively.  $\mathbf{f}$  denotes a body load and  $\mathbf{n}$  is the unit outward normal. Prescribed displacements and tractions are denoted by  $\bar{\mathbf{u}}$  and  $\mathbf{t}$ , respectively. The total boundary is made up of non-overlapping Dirichlet ( $\Gamma_D$ ), Neumann ( $\Gamma_{N,phys}, \Gamma_{N,cont}$ ) and Interface ( $\Gamma_I$ ) parts (see Figure 1)

$$\partial\Omega_{phys} \cap \partial\Omega_{cont} = \Gamma_I \quad (16)$$

$$\Gamma_I \cup \Gamma_D \cup \Gamma_{N,phys} = \partial\Omega_{phys} \quad (17)$$

$$\Gamma_D \cap \Gamma_{N,phys} = \emptyset \quad (18)$$

$$\Gamma_I \cap (\Gamma_D \cup \Gamma_{N,phys}) = \emptyset \quad (19)$$

$$\Gamma_I \cup \Gamma_{N,cont} = \partial\Omega_{cont} \quad (20)$$

$$\Gamma_I \cap \Gamma_{N,cont} = \emptyset. \quad (21)$$

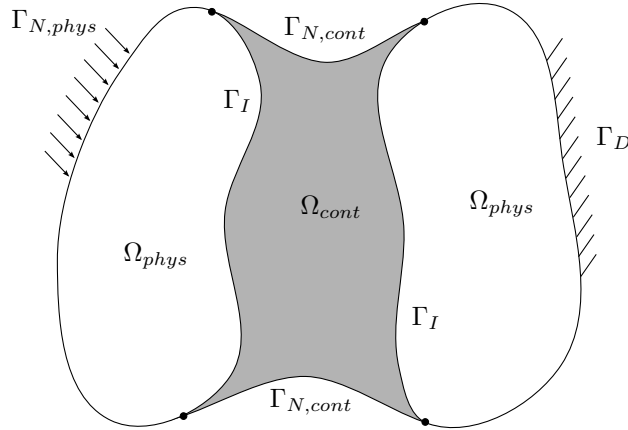


Figure 1: The physical and contact domains,  $\Omega_{phys}$  and  $\Omega_{cont}$ , respectively, are connected via interface boundaries  $\Gamma_I$ . Dirichlet boundaries  $\Gamma_D$  and the Neumann boundaries  $\Gamma_{N,phys}$  only touch the physical domain  $\Omega_{phys}$ . The Neumann boundary  $\Gamma_{N,cont}$  is only part of the contact domain  $\Omega_{cont}$ .

### 3.2. Weak form for the deformation of the physical bodies

The weak form of the physical domain (see also (1)) reads

$$\int_{\Omega_{phys}} \boldsymbol{\sigma}_{phys} : \delta \boldsymbol{\epsilon} \, dv - \int_{\Omega_{phys}} \mathbf{f} \cdot \delta \mathbf{u} \, dv - \int_{\Gamma_N} \mathbf{t} \cdot \delta \mathbf{u} \, ds = 0. \quad (22)$$

In the current paper, physical bodies are either represented by isotropic linear elastic solids or—in the case of large deformations—by hyperelastic, neo-Hookean solids. The latter are described by the strain energy function

$$W_{NH} = \frac{\mu}{2} (\text{tr} \hat{\mathbf{b}} - 3) + \frac{\kappa}{2} (J - 1)^2, \quad (23)$$

where  $\mu$  is the shear modulus,  $\kappa$  is the initial bulk modulus and  $J$  is the Jacobian of the gradient of deformation [37].  $\hat{\mathbf{b}}$  denotes the deviatoric part of the left Cauchy-Green tensor. Hence, the Cauchy stress tensor for the neo-Hookean solids reads

$$\boldsymbol{\sigma}_{phys} = \mu J^{-5/3} (\mathbf{b} - \frac{1}{3} I_b \mathbf{I}) + \kappa (J - 1) \mathbf{I}, \quad (24)$$

where  $I_b$  is the first invariant of the left Cauchy-Green tensor  $\mathbf{b}$ , while  $\mathbf{I}$  is the identity tensor.

### 3.3. Weak form for the deformation of the contact domain

For test functions  $\delta \boldsymbol{\epsilon}$  with support restricted to the contact domain the weak form only contains the contribution of the internal energy. External quantities are omitted by construction (see equation (13))

$$\int_{\Omega_{cont}} \boldsymbol{\sigma}_{cont} : \delta \boldsymbol{\epsilon} \, dv = 0. \quad (25)$$

The contact material used in this work is based on the hyperelastic formulation by Hencky [37]

$$W_H(\lambda_1, \lambda_2, \lambda_3) = \mu \sum_{i=1}^3 (\ln \lambda_i)^2 + \frac{\Lambda}{2} (\ln J)^2, \quad (26)$$

with

$$\ln J = \ln \lambda_1 + \ln \lambda_2 + \ln \lambda_3. \quad (27)$$

Here,  $\lambda_i$  are the principal stretches,  $\mu$  and  $\Lambda$  are the well-known Lamé parameters.

The contact material is introduced as a means of approximately satisfying the Karush-Kuhn-Tucker (KKT) conditions, which relate the normal gap distance  $g$  to the normal reaction force  $R$  in the contact domain [1]:

$$g \geq 0 \quad \text{No normal penetration} \quad (28)$$

$$R \leq 0 \quad \text{Only compressive forces} \quad (29)$$

$$g \cdot R = 0 \quad \text{Consistency requirement.} \quad (30)$$

The material parameters  $\mu$  and  $\Lambda$  are scaled by a small value  $c$ , which will be denoted as contact stiffness in the remainder of this paper. Thus, the principal stresses  $\sigma_{ii}$  obtained from the contact material regularize the KKT conditions, as shown in Figure 2 for the one-dimensional case.

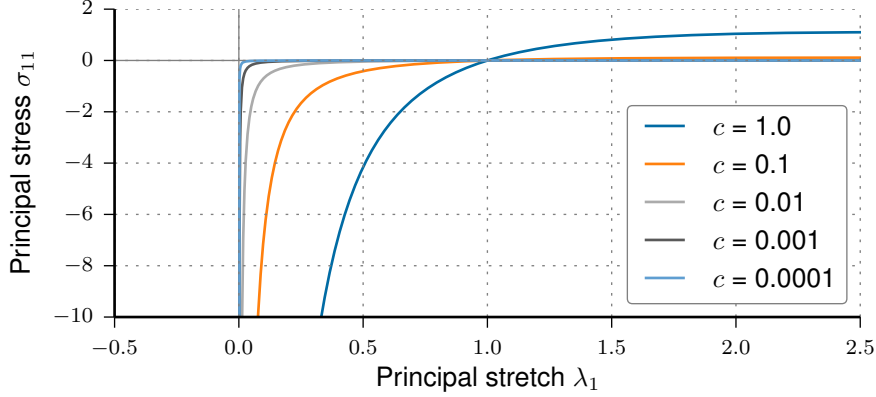


Figure 2: The minimum principal stretch and its corresponding stress are directly related to the gap function  $g$  and the normal reaction force  $R$ , respectively. Hence, the principal stretch can be considered as a normalized gap function. The contact material, thus, regularizes the KKT conditions via scaling of the material parameters using a contact stiffness  $c$  ( $\mu = \Lambda = 1.0$ ).

Here, the stretches  $\lambda_i$  correspond to a normalized gap distance, while the principal stresses  $\sigma_{ii}$

$$\sigma_{ii} = \frac{c}{J} \frac{\partial W_H}{\partial \ln \lambda_i} = \frac{c}{J} (2\mu \ln \lambda_i + \Lambda \ln J) \quad (31)$$

represent the reaction force. Thus, the Cauchy stress tensor for the contact domain reads

$$\boldsymbol{\sigma}_{cont} = \sum_{i=1}^3 \sigma_{ii} \mathbf{n}_i \otimes \mathbf{n}_i. \quad (32)$$

The principal stretches  $\lambda_i$  and their associated directions  $\mathbf{n}_i$  are obtained from the eigenvalue problem [37]

$$(\mathbf{b} - \mathbf{I}\lambda_i^2) \mathbf{n}_i = 0, \quad (33)$$

where  $\mathbf{b}$  is the well-known left Cauchy-Green tensor.

Note that the choice of the parameter  $c$  largely depends on the initial gap between contacting bodies. The larger the initial gap, the earlier small stretch values—and thus significant reaction forces—will be encountered during the load history.

Furthermore, the contact material formulation at hand is frictionless since no energy dissipation is included. Strictly speaking, the formulation is not free of sticking, but the following simplified investigation shows that sticking reactions are orders of magnitudes smaller than the normal reaction forces. Since a tangential gap leads to a shear deformation of the contact domain (see Figure 3), shear stresses are responsible to enforce sticking.

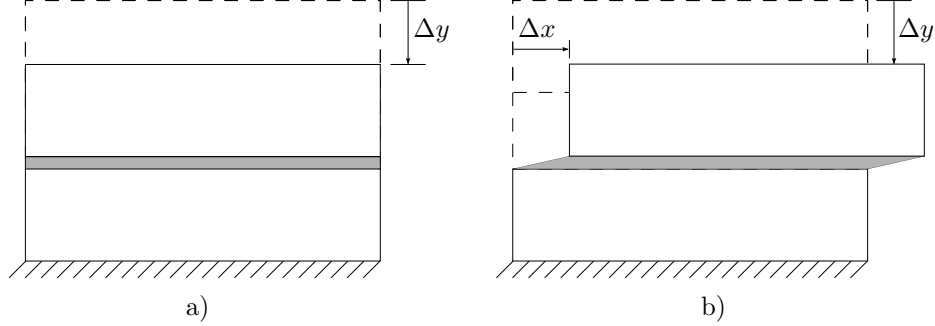


Figure 3: Two physical bodies (white) are connected by a contact domain (gray) containing the contact material formulation. a) Pure compression of the contact domain. b) Relative lateral displacement of the two bodies leads to a shear deformation of the contact domain.

These stresses, however, do not grow substantially during the compression and shear deformation of the contact material, which can be seen in Figure 4. Here, components of the stress tensor are plotted versus the shear parameter  $\gamma$  in a highly compressed contact zone ( $\lambda_{min} = 10^{-4}$ ). This deformation is described by the following deformation gradient

$$\mathbf{F} = \begin{bmatrix} 1 & \gamma \\ 0 & 10^{-4} \end{bmatrix}.$$

The shear component  $\sigma_{xy}$  turns out to be orders of magnitude smaller than the corresponding compression stress  $\sigma_{yy}$ .

#### 3.4. Finite element discretization

The nonlinear equations emerging from the contact material formulation are treated numerically by means of the Newton-Raphson method. To this end, the weak forms given in equations (22) and (25) are first linearized and then discretized using the  $p$ -version of the finite element method as described in Section 2.1. Eventually, the following discrete system of equations emerges for both the physical domain and the contact domain:

$$\left( \mathbf{K}_k^{c,i} + \mathbf{K}_k^{\sigma,i} \right) \Delta \mathbf{u}_k^i = \mathbf{G}_k^i. \quad (34)$$

$\mathbf{K}_k^{c,i}$  and  $\mathbf{K}_k^{\sigma,i}$  are the consistent and geometric parts of the tangential stiffness matrix, respectively, at load step  $i$  and iteration  $k$ .  $\Delta \mathbf{u}_k^i$  is the incremental

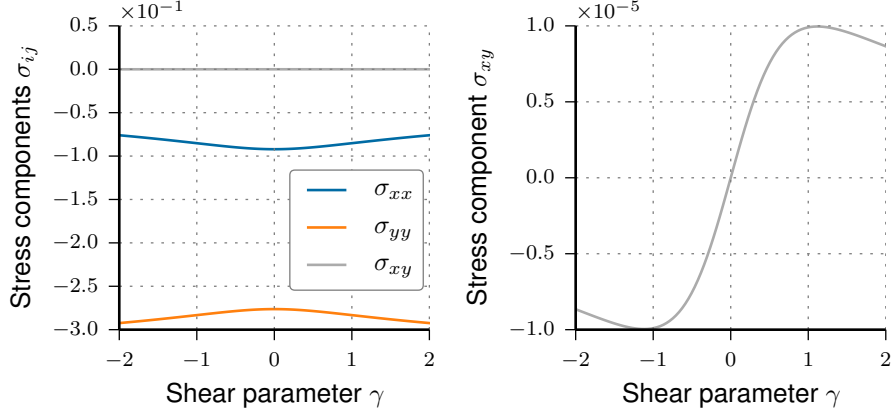


Figure 4: Stress components of the two-dimensional Cauchy stress tensor for an initial compression ( $\lambda_2 = 10^{-4}$ ) of the contact material and a varying shear parameter  $\gamma$ . The shear stress  $\sigma_{xy}$ —shown also in detail on the right—is several orders of magnitude smaller than the component  $\sigma_{yy}$ , which is related to the contact pressure ( $c = 10^{-6}$ ,  $\mu = 1.0$ ,  $\lambda = 1.0$ ).

displacement and  $\mathbf{G}_k^i$  is the residual given as

$$\mathbf{G}_k^i = \mathbf{f}_k^{ext,i} - \mathbf{f}_k^{int,i}, \quad (35)$$

where  $\mathbf{f}_k^{ext,i}$  and  $\mathbf{f}_k^{int,i}$  are the vectors of external and internal virtual work, respectively.

#### 3.4.1. Tangential stiffness

The consistent part of the tangential stiffness matrix is obtained as

$$\mathbf{K}^c = \int_{\Omega_{phys}} \mathbf{B}^T \mathbf{c}_{phys} \mathbf{B} dv + \int_{\Omega_{cont}} \mathbf{B}^T \mathbf{c}_{cont} \mathbf{B} dv, \quad (36)$$

where  $\mathbf{B}$  is the spatial strain operator in Voigt notation and  $\mathbf{c}_{phys}$  and  $\mathbf{c}_{cont}$  are the spatial elasticity tensors for the physical and contact domain, respectively. The spatial elasticity tensor for the neo-Hookean solids [37], is given as

$$\mathbf{c}_{phys}^{NH} = \hat{\mathbf{c}} + \mathbf{c}_p + \mathbf{c}_\kappa. \quad (37)$$

Here  $\hat{\mathbf{c}}$ ,  $\mathbf{c}_p$  and  $\mathbf{c}_\kappa$  are the deviatoric, pressure and volumetric components of the spatial elasticity tensor, respectively:

$$\hat{\mathbf{c}} = 2\mu J^{-5/3} \left( \frac{1}{3} \text{tr} \mathbf{b} \mathbf{i} - \frac{1}{3} \mathbf{b} \otimes \mathbf{I} - \frac{1}{3} \mathbf{I} \otimes \mathbf{b} + \frac{1}{9} I_{\mathbf{b}} \mathbf{I} \otimes \mathbf{I} \right) \quad (38)$$

$$\mathbf{c}_p = \kappa (J - 1) (\mathbf{I} \otimes \mathbf{I} - 2\mathbf{i}) \quad (39)$$

$$\mathbf{c}_\kappa = \kappa J (\mathbf{I} \otimes \mathbf{I}). \quad (40)$$

The quantity  $\mathbf{i}$  is the fourth-order identity tensor defined as

$$\mathbf{i} = \frac{1}{2} (\delta_{ik}\delta_{jl} + \delta_{il}\delta_{jk}). \quad (41)$$

For the physical bodies containing the isotropic linear elastic material, the consistent stiffness matrix is evaluated in the undeformed configuration by using the linear elasticity tensor [37].

Following from (26), the spatial elasticity tensor of the contact material is formulated in terms of principal stretches [37]. The Cartesian components of the elasticity tensor are thus defined as

$$\begin{aligned} c_{cont,ijkl} = & \sum_{i,j=1}^3 \frac{c}{J} (2\mu\delta_{ij} + \Lambda) \mathbf{n}_{ijjj} - \sum_{i=1}^3 2\sigma_{ii}\mathbf{n}_{iiii} \\ & + \sum_{\substack{i,j=1 \\ i \neq j}}^3 \frac{\sigma_{ii}\lambda_j^2 - \sigma_{jj}\lambda_i^2}{\lambda_i^2 - \lambda_j^2} (\mathbf{n}_{ijij} + \mathbf{n}_{ijji}), \end{aligned} \quad (42)$$

with

$$\mathbf{n}_{ijkl} = \mathbf{n}_i \otimes \mathbf{n}_j \otimes \mathbf{n}_k \otimes \mathbf{n}_l. \quad (43)$$

The geometric part of the tangential stiffness matrix that connects degrees of freedom  $a$  and  $b$  reads

$$\mathbf{K}_{ab}^\sigma = \int_{\Omega_{phys}} (\nabla N_a \cdot \boldsymbol{\sigma}_{phys} \nabla N_b) \mathbf{I} dv + \int_{\Omega_{cont}} (\nabla N_a \cdot \boldsymbol{\sigma}_{cont} \nabla N_b) \mathbf{I} dv, \quad (44)$$

where  $\nabla N_i$  is the gradient of the shape function for degree of freedom  $i$ , while  $\boldsymbol{\sigma}_{phys}$  and  $\boldsymbol{\sigma}_{cont}$  are the stress tensors for the physical and contact domain, respectively. Note that the contribution for the geometric stiffness vanishes for linear elastic physical bodies. This is due to the fact that, here, the variation of the strain tensor is not a function of the current deformation [37].

### 3.4.2. Discretized external and internal virtual work

The residual is defined as the difference of external and internal work (35). Here, the vector of external virtual work is only defined for the physical part of the domain

$$\mathbf{f}^{ext} = \int_{\Omega_{phys}} \mathbf{N}^T \mathbf{f} dv + \int_{\Gamma_{N,phys}} \mathbf{N}^T \mathbf{t} dv, \quad (45)$$

where the first term stands for the virtual work introduced in  $\Omega_{phys}$  by a source term  $\mathbf{f}$ . The second term represents the natural boundary conditions for an applied traction  $\mathbf{t}$  along  $\Gamma_{N,phys}$  (see Figure 1). The vector of internal virtual work is given as

$$\mathbf{f}^{int} = \int_{\Omega_{phys}} \mathbf{B}^T \boldsymbol{\sigma}_{phys} dv + \int_{\Omega_{cont}} \mathbf{B}^T \boldsymbol{\sigma}_{cont} dv, \quad (46)$$

where the Cauchy stress tensors for the physical domain  $\boldsymbol{\sigma}_{phys}$ , and the contact domain  $\boldsymbol{\sigma}_{cont}$  are given in equations (24) and (32), respectively.

### 3.5. A line-search method to prevent element collapse inside the contact domain

The inherent non-linearity of contact problems is reflected in the non-linearity of the contact material formulation at hand. The solution is obtained using the full Newton-Raphson method. Since the contact material is highly compliant at the beginning of the load history, it can happen that displacement increments are computed that cause an overlap of adjacent contact boundaries. For classical formulations, such as the penalty or Lagrange multiplier method, this poses no further difficulty, as penetrations are removed in the succeeding iterations. Yet, the approach at hand can be classified as a barrier-type approach, which is why the solution has to be admissible at all times. To this end, measures must be taken to ensure that adjacent contact interfaces do not interpenetrate. A straightforward approach would be to cut load increments if such a case is detected (e.g. by evaluating the determinant of the deformation gradients at integration points). Since this could lead to a very small load increment and, in consequence, to a significant increase in computation time, we utilize an inexact line search based on the aforementioned determinant of the deformation gradient:

$$\Delta \mathbf{u}_{k,m+1}^i = \Delta \mathbf{u}_{k,m}^i - \frac{f_m}{f_m - f_{m-1}} \cdot (\Delta \mathbf{u}_{k,m}^i - \Delta \mathbf{u}_{k,m-1}^i) \quad (47)$$

$$f_m = \min (\det \mathbf{F}_{k,m}^i(\mathbf{X}_q)), \forall \mathbf{X}_q \in \Omega_{cont}. \quad (48)$$

Here,  $\Delta \mathbf{u}_{k,m}^i$  denotes the modified displacement increment at load step  $i$ , Newton iteration  $k$  and line search sub-iteration  $m$ . The quantity  $f_m$  is the minimum of all determinants of the gradient of deformation  $\mathbf{F}$  at the integration points  $\mathbf{X}_q$  in the contact domain  $\Omega_{cont}$  at sub-iteration  $m$ .

A combined stopping criterion is employed, taking into account the change of the modified displacement increment and the resulting minimum of the all determinants of  $\mathbf{F}$ :

$$[(\|\Delta \mathbf{u}_{k,m+1}^i - \Delta \mathbf{u}_{k,m}^i\| < \epsilon_\Delta) \vee (\|f_{m+1}\| < \epsilon_f)] \wedge (f_{m+1} > 0). \quad (49)$$

Here,  $\epsilon_\Delta$  and  $\epsilon_f$  are stopping tolerances for the change of solution increment and the absolute value of  $f$ , respectively. In the paper at hand both tolerances have been set to  $10^{-6}$ .

While the proposed line-search works well for all the examples investigated in this study, there might also be cases that require other means—such as automatic increment cutting, for example—to obtain a feasible solution (see e.g. [21, 47]). However, we will show that cutting increments alone might not suffice if the contact stiffness is too low (see section 4.1.2).

## 4. Numerical results

In this section the capabilities of the proposed contact formulation are investigated by means of different numerical examples.

#### 4.1. A large deformation model problem including self-contact

First, the influence of different parameters will be investigated using a two-dimensional model problem in the large deformation regime. These parameters include the ansatz order  $p$  and the order of integration  $q$  inside the contact domain as well as the contact stiffness  $c$ , as defined in Section 3.3. Furthermore, the contact material formulation will be compared to a classical  $h$ -FEM formulation using the commercial FEM-package ANSYS<sup>1</sup>.

##### 4.1.1. Definition of the model problem

The model problem under consideration is a rectangular block with a slotted hole subjected to a constant, vertical load as depicted in Figure 5. The physical part shown in white contains the neo-Hookean material for the plane-strain state, equation (37), whereas the slot (gray) is filled with the contact material model given in equation (42). Fillets at the corners of the slot will be treated according to the finite cell method as described in Section 2.2. All boundary parts that may come into contact are discretized conformingly, i.e. element edges match the boundaries exactly. The total load will be applied in 10 uniform, incremental steps.

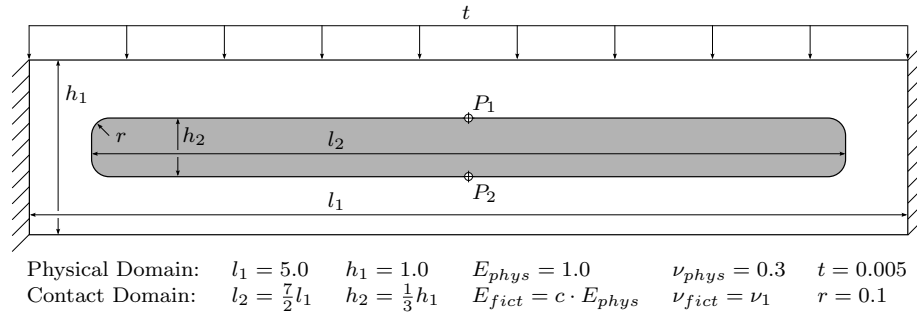


Figure 5: Model problem setup: Rectangular block with a slotted hole fully supported at both sides and subjected to a vertical, distributed load. The physical domain (white) contains the neo-Hookean material introduced in Section 3.2. The slotted hole (gray) is filled with the contact material described in Section 3.3.

##### 4.1.2. Choice of the polynomial degree in the contact domain

The aim of this first analysis is to examine the influence of the high order shape functions inside the contact domain. To this end, the model problem introduced in the previous section is solved using different ansatz orders. Figure 6 shows the evolution of the residual measure obtained in the Newton-Raphson method versus the cumulative number of iterations for different polynomial degrees and a contact stiffness of  $c = 10^{-6}$ .

<sup>1</sup>ANSYS®, Academic Research, Release 14.5

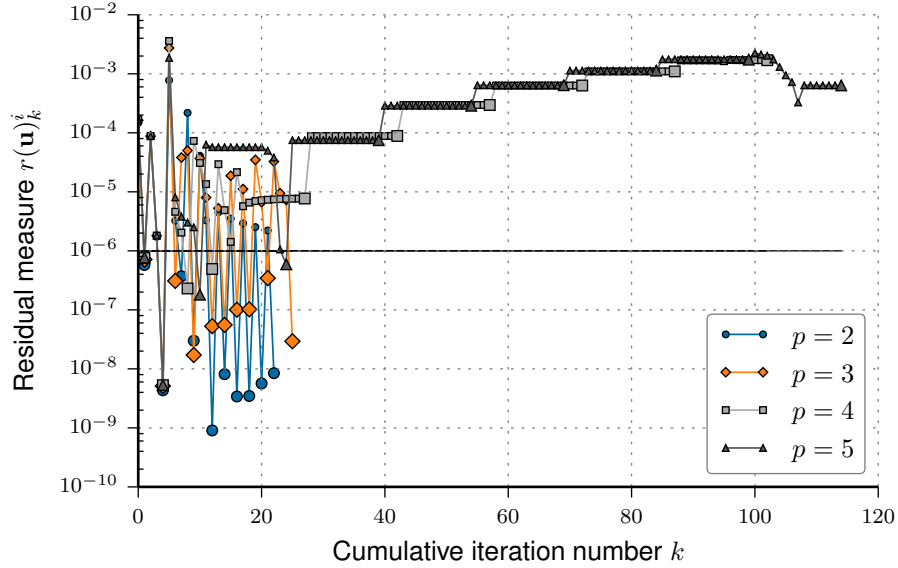


Figure 6: Convergence progress of Newton-Raphson method for uniform ansatz orders throughout the computational domain. The total load was applied in 10 equally sized steps. Intermediate and final iterations for each load increment, including possible line searches, are depicted by dedicated small and large markers, respectively. The convergence tolerance for the Newton solver was set to  $10^{-6}$ . The maximum number of iterations for all computations was restricted to 15 iterations.

The residual measure used here is defined as

$$r(\mathbf{u})_k^i = \sqrt{\mathbf{G}_k^i \cdot \Delta \mathbf{u}_k^i}, \quad (50)$$

where  $\mathbf{G}_k^i$  and  $\Delta \mathbf{u}_k^i$  are the residual (35) and the solution increment at load step  $i$  and iteration  $k$ , respectively. The convergence tolerance for the Newton solver was set to  $10^{-6}$ . When applying the same ansatz order in the physical domain and the contact domain, the final solution only converges up to the desired tolerance for  $p = 2$  and  $p = 3$ . The contact stiffness in this analysis is rather low ( $c = 10^{-6}$ ), and the elements in the middle are extremely compressed (see Figure 7).

Minor perturbations in the numerical solutions might lead to an invalid state, i.e. the elements collapse locally, and the respective Jacobians of the deformation gradient become negative. This is of course likely to happen during the discrete steps made during the Newton iterations. The line search proposed in section 3.5 tries to avoid this by reducing the current increment. However, the resulting configuration might not be close enough to the equilibrium state. Obvious possibilities to overcome this problem are an increase of the contact stiffness as can be seen from Figure 8 or the reduction of the load increment.

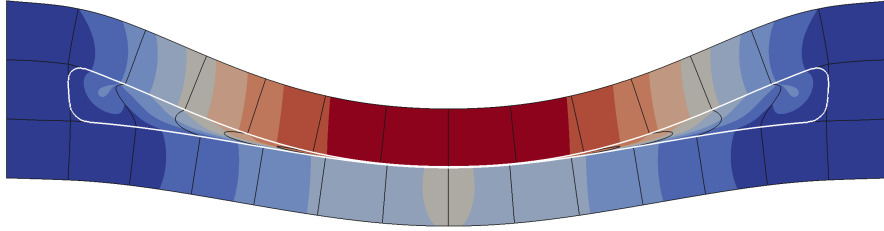


Figure 7: Displacement solution of the model problem for the highest ansatz order that converged ( $p = 3$ ). The highly deformed edges inside the contact domain are clearly visible.

The latter approach does not immediately lead to stable results for the given

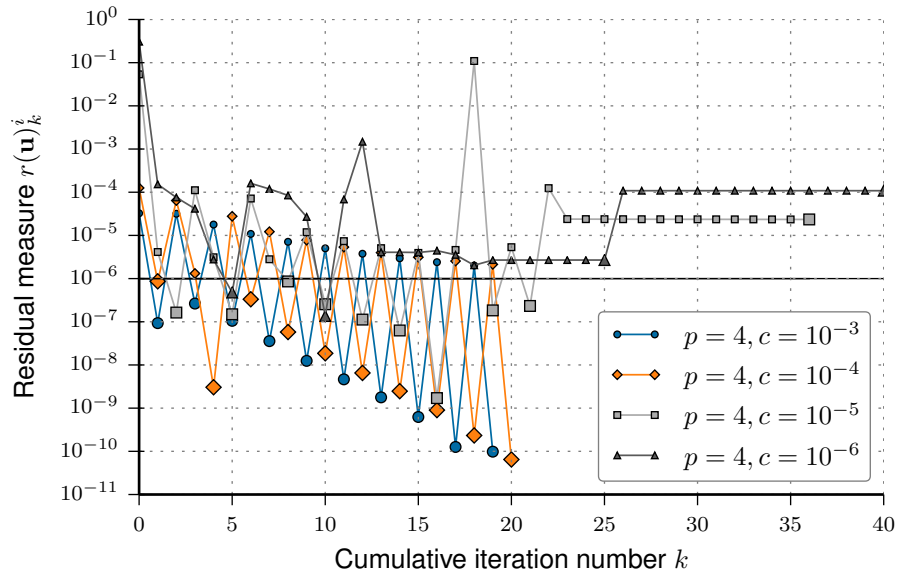


Figure 8: Convergence progress for different contact stiffnesses  $c$  and a uniform ansatz order of  $p = 4$  in all elements. Intermediate and final iterations for each load increment, including possible line searches, are depicted by dedicated small and large markers, respectively. The maximum number of iterations is set to 15.

contact stiffness of  $c = 10^{-6}$ , as can be seen in Figure 9. However, if the contact stiffness is reduced to  $c = 10^{-5}$ , smaller load increments lead to converging results at the cost of a much higher number of computations (see Figure 10).

A third alternative is the deactivation of the high order modes inside the contact domain, which is illustrated for the two-dimensional case in Figure 11. The goal of the simulation is not a good approximation of the deformation state in the fictitious contact domain, but the reaction in normal direction to

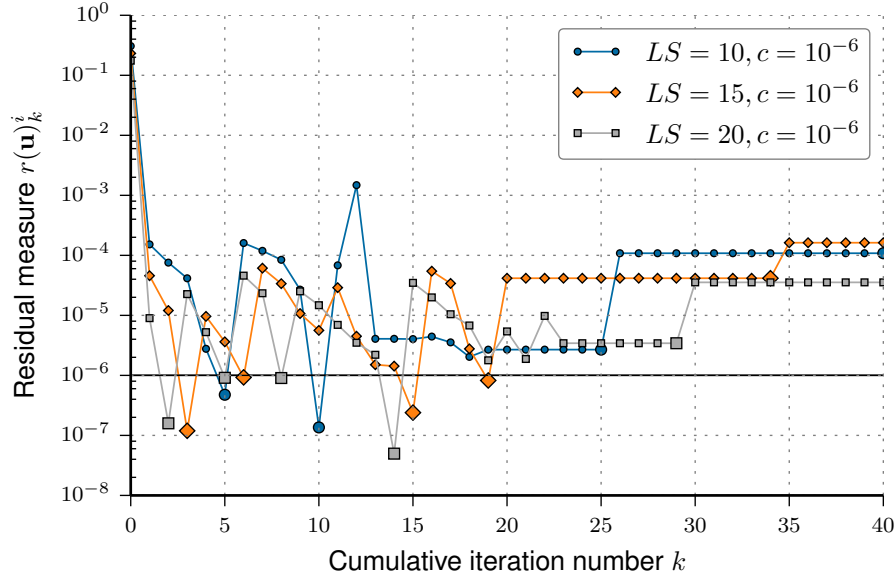


Figure 9: Convergence progress for a different number of load steps  $LS$ , a uniform ansatz order of  $p = 4$  in all elements and a contact stiffness of  $c = 10^{-6}$ . Intermediate and final iterations for each load increment, including possible line searches, are depicted by dedicated small and large markers, respectively. The maximum number of iterations for all computations was restricted to 15 iterations.

the contact boundaries. By deactivating high order modes inside the contact domain, physical interfaces can still deform according to their high polynomial degree and the robustness of the solution is drastically improved (see Figure 12). Also, the deactivation does not impose an overhead. On the contrary, it lies in line with the usual implementation of hierarchic shape functions in which different polynomial orders may be assigned to edges, faces and volumes. To ensure continuity, adjacent edges (or faces in 3D) are set to the highest degree of all involved entities. Therefore, it is only necessary to set all modes of the elements within the contact domain to  $p=1$ , and the rest can be handled by the standard routines to ensure compatibility. Additionally, the total number of degrees of freedom is reduced, which has a positive effect on the computational efficiency, see Figure 13.

Since this modification allows us to use larger and thus fewer load increments and also reduces the total number of degrees of freedom (see Figure 13), we apply this approach in all of the following examples.

#### 4.1.3. Influence of integration order $q$ on minimum contact gap $g_{min}$

Classical approaches for the simulation of contact problems usually track the status of contact at discrete points [1]. The current approach evaluates

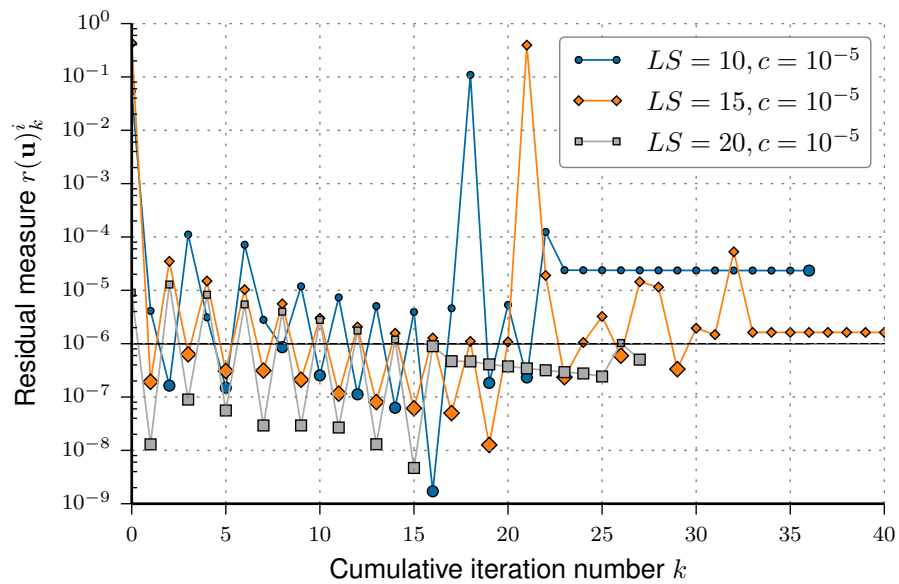


Figure 10: Convergence progress for a different number of load steps  $LS$ , a uniform ansatz order of  $p = 4$  in all elements and a contact stiffness of  $c = 10^{-5}$ . Intermediate and final iterations for each load increment, including possible line searches, are depicted by dedicated small and large markers, respectively. The maximum number of iterations for all computations was restricted to 15 iterations.

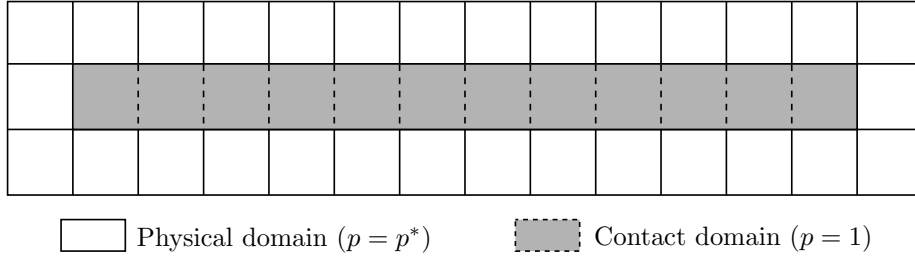


Figure 11: The domain of the model problem given in Section 4.1.1 is discretized by  $14 \times 3$  high order finite elements. All higher modes (i.e. edge and face modes) of elements, which are fully or partially in the contact domain (gray), are deactivated. Edge modes touching the physical and the contact domain remain active.

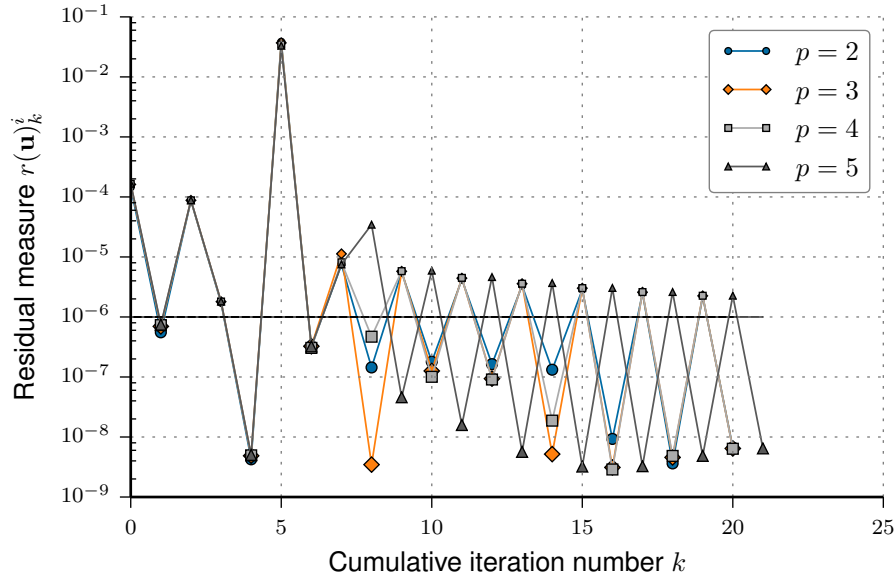


Figure 12: Convergence progress of Newton-Raphson method for modified ansatz orders inside the contact domain. If high order modes inside the contact domain are deactivated, the solution converges to the desired tolerance for all ansatz orders. The total load was applied in 10 equally sized steps. Intermediate and final iterations for each load increment, including possible line searches, are depicted by dedicated small and large markers, respectively. The convergence tolerance for the Newton solver was set to  $10^{-6}$ .

the principal stretches at integration points during the numerical integration of the discretized weak form. Contact is established, if one of the principal stretches approaches zero. Thus, the integration points act as sampling points for contact detection. Therefore, the influence of the number of integration points on the resulting contact gap is investigated. To this end, the gap is

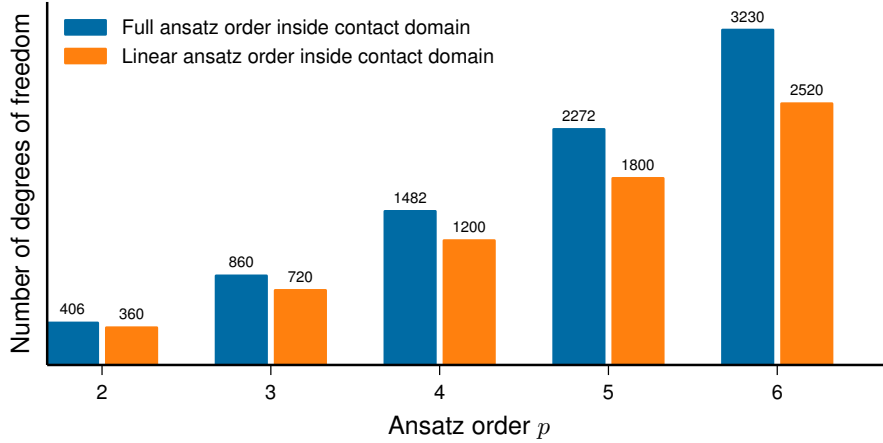


Figure 13: Modifying the ansatz orders inside the contact domain (light blue bars) reduces the total number of degrees of freedom and, thus, has the additional benefit of saving computational costs.

computed for different orders of numerical integration  $q$  and for different ansatz orders  $p$ . Note that the ansatz orders are only varied inside the physical domain (see Section 4.1.2). All computations draw on the standard Gauss-Legendre scheme. The contact gap is measured as the distance between the points  $P_1$  and  $P_2$  (Figure 5). Results were computed using a contact stiffness of  $c = 10^{-6}$ .

The obtained minimum contact gaps ( $g_{min}$ ) normalized by the initial gap ( $g_0 = 1/3$ ) are summarized in Table 1. The results show that the normalized

Table 1: Influence of the integration order  $q$  on the resulting contact gap  $g$  ( $c = 10^{-6}$ ).

$p = 2$		$p = 3$		$p = 4$	
$q$	$g_{final}/g_0[\%]$	$q$	$g_{final}/g_0[\%]$	$q$	$g_{final}/g_0[\%]$
3	3.97008949146	4	4.00308944753	5	4.01568941207
4	3.96618949065	5	4.00578943907	6	4.01688941207
5	3.97008949146	6	4.00698943907	7	4.01568940280
6	3.97128949146	7	4.00578943907	8	4.01598941207
7	3.97008949146	8	4.00608943907	9	3.96138927748

contact gaps remain close to 4% for the investigated configurations.

For this setup, the order of integration does not have a significant influence on the resulting minimum contact gap, and should thus only be governed by the polynomial degree  $p$  to precisely integrate the element matrices. We will

further investigate the influence of the integration order on contact detection for a setup involving curved boundaries in a later section.

#### 4.1.4. Influence of contact stiffness $c$ on minimum contact gap $g_{min}$

Considering again the example setup depicted in Figure 5, the influence of the contact stiffness  $c$  on the minimum contact gap  $g_{min}$  shall be investigated. This is a study on the *model error*, as obviously even the exact solution using a contact domain with a finite  $c$  corresponds to a slightly different physical model. Figure 14 depicts the ratios of the resulting minimal gap  $g_{min}$  and the initial gap  $g_0$  for ansatz orders  $p = 2, 3, 4$ . As can be seen, the ratios approach zero as the contact stiffness  $c$  is reduced. Also, the difference between the ratios computed with different ansatz orders is negligible. The contact material therefore converges to the limit state defined by the Karush-Kuhn-Tucker conditions for normal contact, as outlined in Section 3.3. Furthermore, the gap ratios for a contact stiffness of  $c = 10^{-5}$  are already in the range of 10%, which is sufficient for many engineering applications. The gap ratios can also be reduced to a range of 1% by choosing  $c = 10^{-6}$ .

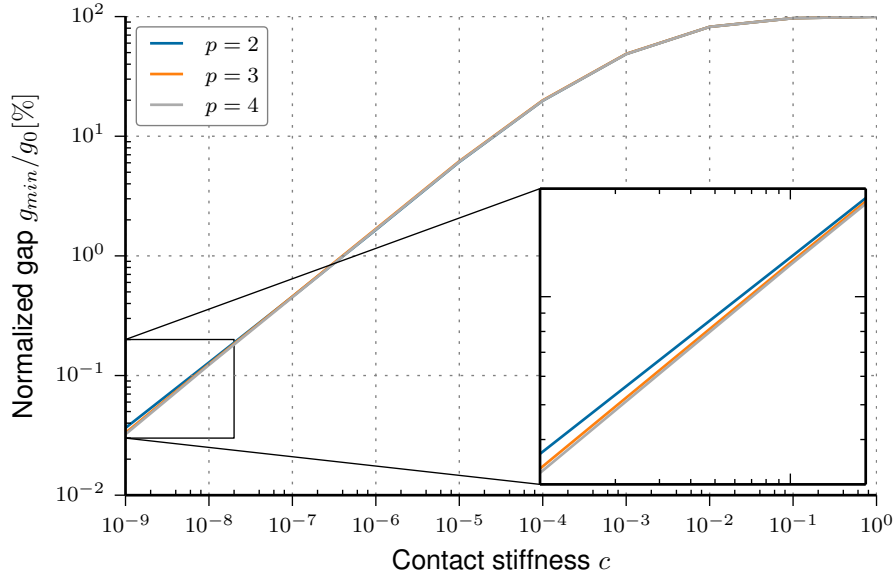


Figure 14: Contact stiffness  $c$  vs. ratio of minimum contact gap  $g_{min}$  and initial gap  $g_0$ . Results have been obtained for ansatz orders  $p = 2, 3, 4$ .

#### 4.1.5. Equivalent von Mises stresses $\sigma_m$ compared to a classical $h$ -FEM formulation

The following example serves to compare the stress solution of the setup depicted in Figure 5 with a simulation conducted with ANSYS (see Section 4.1.6).

The latter uses 1600 quadratic elements of type *PLANE183* [48]. The results for the contact material ( $p = 5$ ) and ANSYS are shown in Figures 15 and 16, respectively. Both simulations result in similar stress distributions. However, the analysis using the contact material (1800 degrees of freedom) uses far less degrees of freedom, than the ANSYS simulation (10.480 degrees of freedom).

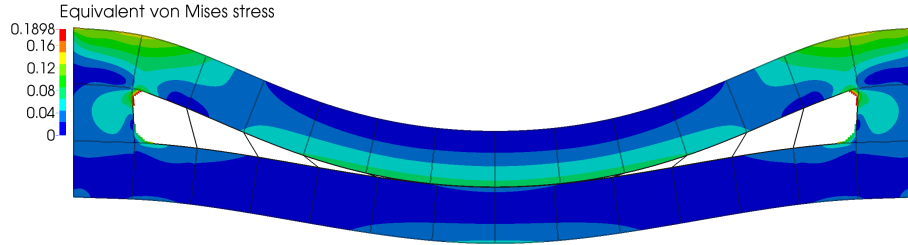


Figure 15: Equivalent von Mises stresses obtained using the contact material ( $p = 5$ ).

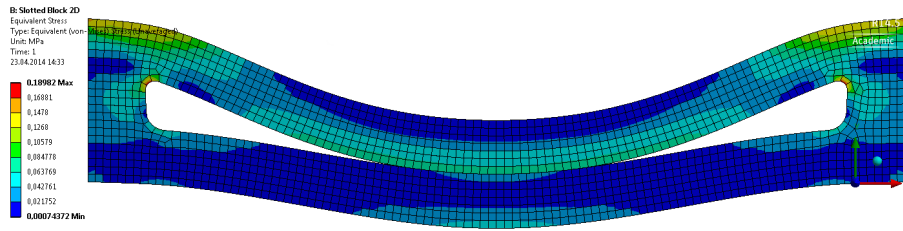


Figure 16: Equivalent von Mises stresses obtained by ANSYS.

#### 4.1.6. Comparison of normal pressures $p_N$

In the following, the normal contact pressures  $p_N$  computed with the contact material are compared with the values obtained by the ANSYS simulation (see Figure 16).

The pressures for the contact material are obtained by evaluating the stress tensor  $\sigma$  and the normals  $\mathbf{n}$  along the points of a segmented line (10000 segments) on the lower contact interface (see Figure 5). The normals are not continuous along the discrete line segments. Hence, the average of the two segment normals is taken for every evaluation point connecting two line segments. The normal pressure is then computed as:

$$p_N = \sigma_{ij} n_i n_j. \quad (51)$$

The graphs of both the  $h$ -FEM and the contact material results show the same general behavior, with similar values of normal contact pressure. The contact material pressures converge with decreasing contact stiffness  $c$ , leading to a much smoother distribution than the ANSYS results. The  $h$ -FEM simulation is

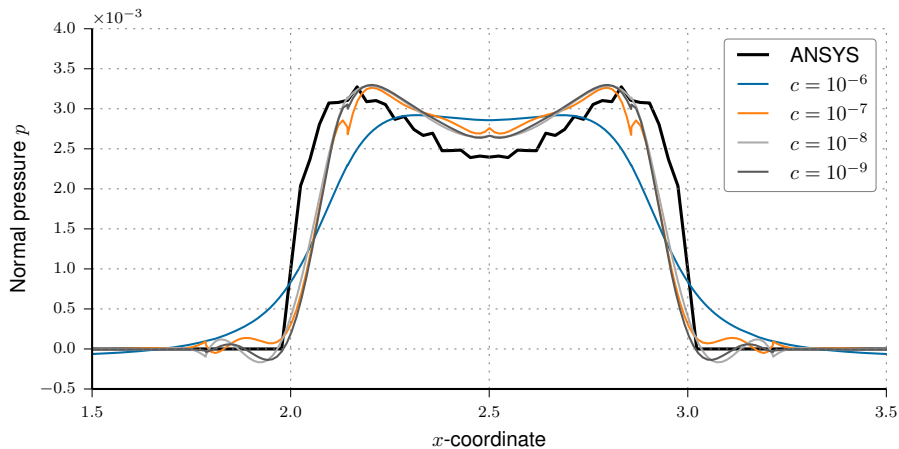


Figure 17: Comparison of resulting normal pressures  $p_N$  for different contact stiffnesses  $c$  with results obtained using ANSYS. The ansatz order is set to  $p = 5$ .

able to represent the kink at the contact boundary, while the  $p$ -FEM solutions show slight oscillations at the ends of the contact zone. This is a characteristic inherent to the  $p$ -version, but can be treated by different means including  $r$ -extension [16, 49] or  $hp$ -adaptivity [50, 51]. However, this is beyond the scope of this work.

#### 4.2. Two-dimensional Hertzian contact

In this second example, we consider the Hertzian frictionless contact problem between an infinitely long elastic cylinder and a rigid surface [52]. The cylinder is modelled using a linear elastic, plane strain model of thickness one (see Figure 18). Utilizing symmetries only a quarter of the cylinder is represented. Symmetry boundary conditions are applied in the  $y$ - $z$ -plane. Following Franke et al. [18], the point load of the Hertzian model is represented by a constant prescribed displacement  $\hat{u}_y$  at the horizontal center line of the cylinder. Franke et al. showed that this assumption is valid and that the resulting modelling error is negligible. The circular boundary is represented exactly using the blending function method [53]. Following this approach allows to discretize the geometry with a minimal number of five coarse high-order elements. Note that the mesh is constructed in such a way that the smallest element is 25% wider than the analytically computed contact width  $b$ :

$$b = \sqrt{\frac{4 \cdot F \cdot r}{\pi \cdot \bar{E}}}. \quad (52)$$

This corresponds to the case where only a rough estimate is available of the final contact zone.

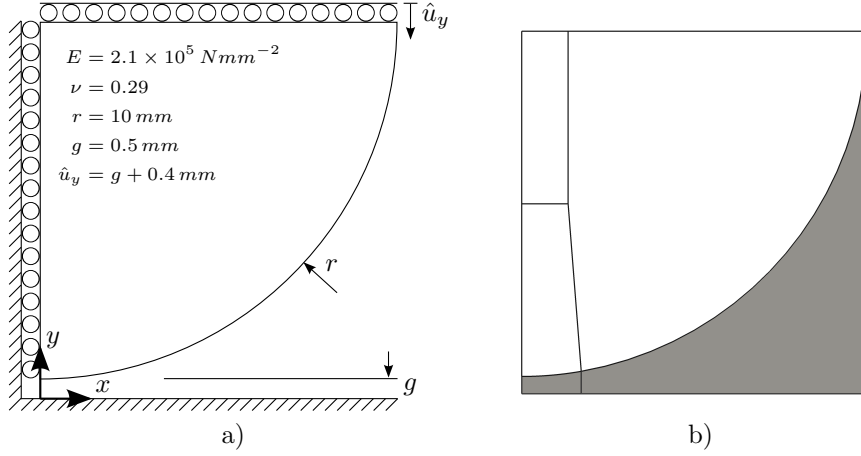


Figure 18: a) Setup for the Hertzian contact problem between an elastic cylinder and a rigid surface. b) Discretization for the contact material approach: elements containing the physical and contact material domain are depicted in white and gray, respectively. The circular boundaries are represented exactly using the blending function method [53].

#### 4.2.1. Contact normal pressure and stress distribution

Following [52], the distribution of the normal pressure for the problem at hand is given by

$$p(x) = p_{max} \cdot \sqrt{1 - \frac{x^2}{b^2}}, \quad (53)$$

where the maximum pressure  $p_{max}$  is

$$p_{max} = \sqrt{\frac{F \cdot \bar{E}}{\pi \cdot r}} \quad \text{with} \quad \bar{E} = \frac{E}{1 - \nu^2}. \quad (54)$$

The normal pressure distribution along the circular boundary is depicted in Figure 19 for different contact stiffnesses and different polynomial degrees. The results are compared with the analytical solution of the Hertzian theory, for which the point load was obtained by integrating the stress component  $\sigma_{yy}$ , computed with  $p = 20$  and  $c = 10^{-6}$ , along the upper edge of the model. The contact material pressures correspond well with the Hertzian distribution in the interior of the contact zone. For higher contact stiffnesses, the numerical solution regularizes the kink of the analytical solution. For lower contact stiffnesses, the solution follows the analytical solution much better—although it does show oscillations around the contact boundary. Similar results have been reported by Franke et al. [16]. Again, these results can be significantly improved by e.g. employing node relocation ( $r$ -FEM) [18, 49] or adaptive hierarchical refinements [50, 51]. However, this is beyond the scope of this work.

Figure 20 depicts the global stress solution obtained with the contact material for ansatz orders  $p = 5$  and  $8$ . As reference, results are provided using a

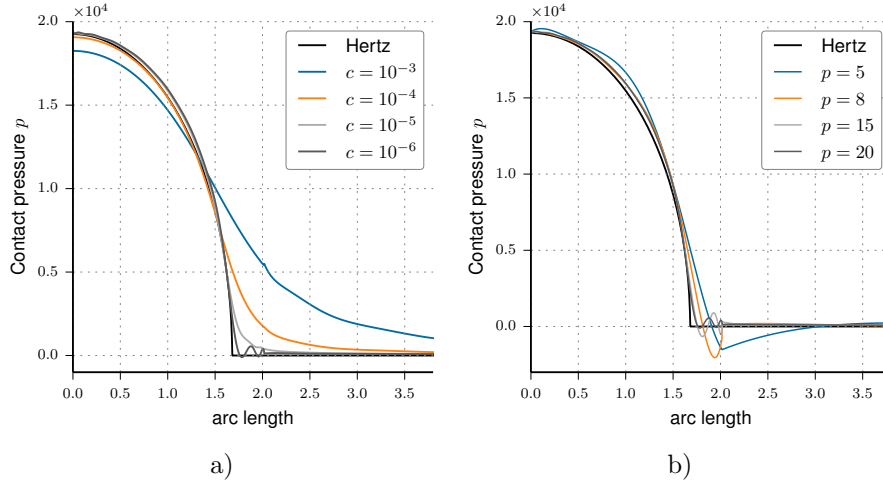


Figure 19: Normal contact pressure computed for a) different contact stiffnesses and a polynomial degree of  $p = 20$  and b) different polynomial degrees and a contact stiffness of  $c = 10^{-6}$ . For reference, the Hertz solution is given for a point load of  $50810N$ .

mesh of  $p = 20$  where the closest node has been moved to the analytical contact boundary. The resulting distributions are typical for the current setup, see e.g. Franke [54]. They show, that good global stress solutions can be obtained already for moderate ansatz orders.

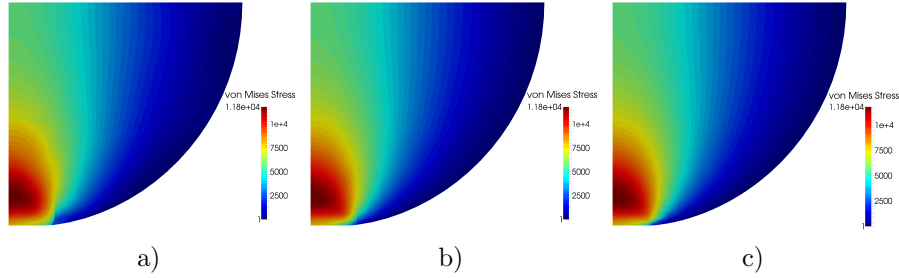


Figure 20: Stresses computed using the contact material. Results are shown for ansatz orders a)  $p = 5$  and b)  $p = 8$ . As reference, results are provided for c)  $p = 20$  using a mesh where the closest node has been moved to the analytical contact boundary.

#### 4.2.2. Integration order for strongly curved contact zones

The influence of the number of integration points was already investigated for the large deformation example in Section 4.1.3, where no significant influence on the final gap could be observed. Now, the case of large elements with a high curvature is investigated. Therefore, we consider the previous setup in its

full configuration—without utilizing symmetry conditions—and a much larger central element. This is depicted in Figure 21 together with a displacement solution using an ansatz order of  $p = 3$  and an integration order of  $q = 4$ . Since there are no integration points in the center, the contact boundary penetrates the rigid target. Hence, the violation of the penetration condition is not fully resolved by the given integration order. For this special setup, this could easily be circumvented by an odd integration order. Figure 22 shows this nicely. Here, the gap value  $g$  at the center line of the model is plotted for a fixed ansatz order of  $p = 3$  but with different orders of integration  $q$ . All the gap values for the even integration orders are negative but converge to zero. Odd integration orders avoid a penetration altogether and lead to much smaller gap values with little variance. It yet needs to be noted that this 'even-odd-peculiarity' is due to the special construction of this example, where the contact is exactly symmetric w.r.t. the midpoint of the corresponding element edge. A general remedy is to use a higher integration order in the elements containing contact material.

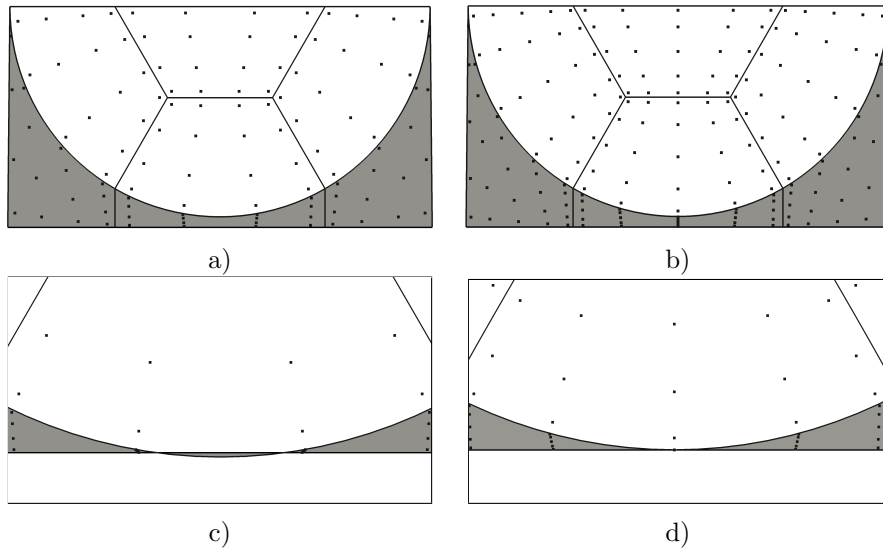


Figure 21: Mesh and integration points for integration order a)  $q = 4$  and b)  $q = 5$ . Physical and contact domain are depicted in white and gray, respectively ( $E = 1.0$ ,  $\nu = 0.3$ ,  $\hat{u}_y = -0.6$ ,  $c = 10^{-4}$ ). c) Detail of the final deformed configuration using an ansatz order of  $p = 3$  and  $q = 4$ . The penetration is clearly visible. d) For an odd integration order (here  $q = 5$ ) no penetrations occur.

#### 4.3. A 3D example: elastic buffer element with multiple self-contact

The following example covers multiple self-contact in a three-dimensional setting. An elastic buffer element consisting of several thin-walled layers is subjected to a distributed, vertical surface load as shown in Figure 23.

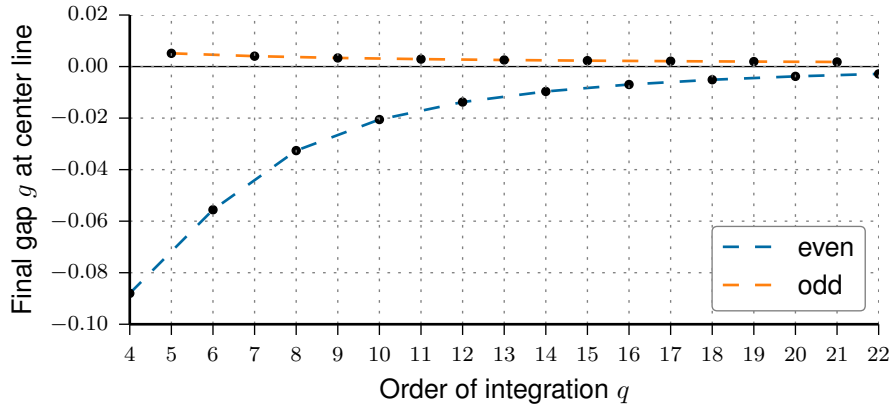


Figure 22: Final gap  $g$  at the center line of the model shown in Figure 21 versus integration order  $q$ . The initial gap was set to  $g = 0.5$  and the radius to  $r = 10$  ( $E = 1.0$ ,  $\nu = 0.3$ ,  $\hat{u}_y = -0.6$ ,  $c = 10^{-4}$ ).

The geometry of this buffer element is embedded in a mesh of finite cells of ansatz order  $p = 5$  (Figure 24). All cavities and fillets are considered at the integration level as explained in Section 2.2 (see Figure 24). Thus, it is possible to represent the small geometric features of the structure—such as the fillets—without explicitly meshing them.

The evolution of the solution is depicted in Figure 25. The results show that the current method is able to reproduce the self-contact as well as the complex state of deformation in the elastic buffer. Furthermore, the equivalent von Mises stresses obtained from the contact material are compared to a simulation performed with ANSYS, see Figures 26 and 27, respectively. The simulation using the contact material approach was performed with 18,990 degrees of freedom, whereas the ANSYS simulation employed quadratic hexahedra of type *SOLID186* and *SOLID187* [48], leading to 84,195 degrees of freedom. Although the contact material approach only uses one fourth of the number of DOFs of the ANSYS solution, both results show the same characteristic stress distribution. Even if the contact formulation in our implementation is far from being optimized, the computational time is in the same order as the one for the ANSYS simulation. This again demonstrates the capabilities of high order finite elements.

## 5. Conclusion

This paper presents an alternative method for the simulation of frictionless contact problems. The new approach combines a contact material formulation and the  $p$ -version of the finite element method. Contact constraints are enforced on the domain level by embedding the physical structure in a contact material,

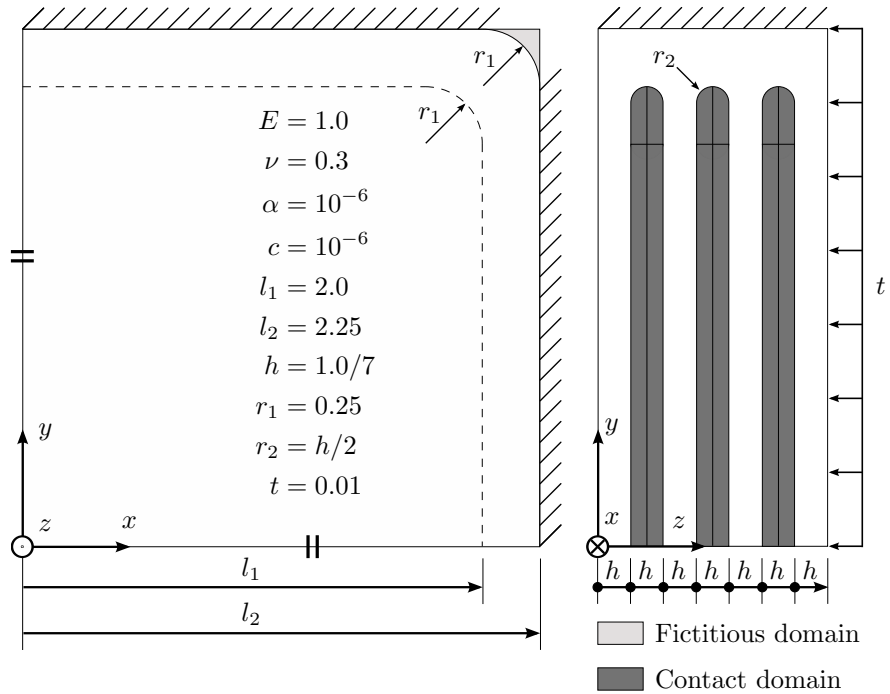


Figure 23: Schematic setup of complex 3D example: Elastic buffer element with multiple self-contact. The material parameters of the fictitious domain (light gray) as well as the contact domain (dark gray) are scaled by the parameters  $\alpha$  and  $c$ , respectively. Exploiting symmetries along the  $x$ - and  $y$ -directions, the numerical model only considers a quarter of the damper, as shown.

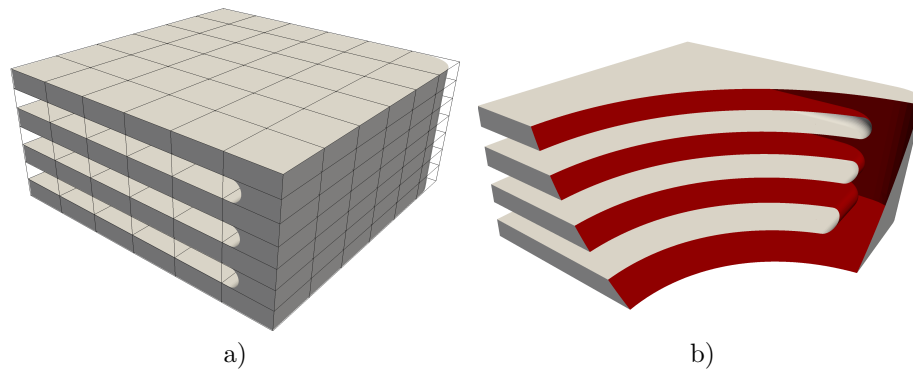


Figure 24: a) The buffer is embedded in a structured Cartesian grid of  $6 \times 6 \times 7$  high order finite elements ( $p = 5$ ). b) A cut view of the boundary representation of the buffer. Inner fillets and cavities are recovered at the integration level as outlined in Section 24.

which prevents adjacent contact boundaries from interpenetrating. The proposed material is based on the hyperelastic formulation by Hencky, which uses

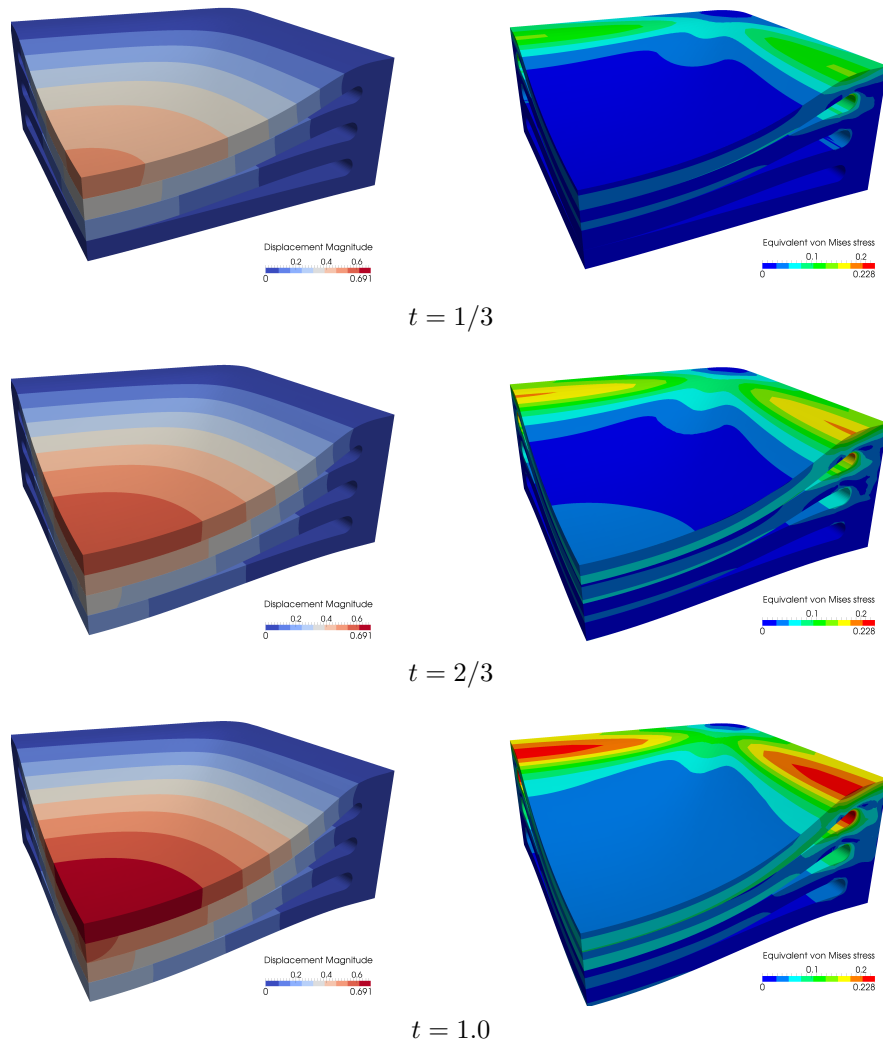


Figure 25: Load history depicting the displacement magnitude (left) and equivalent von Mises stress (right) for different load steps.

a logarithmic strain measure and regularizes the Karush-Kuhn-Tucker conditions by scaling the material parameters.

To avoid penetration of contact interfaces, a line search method was utilized that evaluated the determinant of the gradient of deformation inside the contact domain.

The applicability of the method was demonstrated by means of two- and three-dimensional examples, including a Hertzian contact example.

The application of high ansatz orders led to results comparable to classical approaches in the physical domain for only a small number of coarse elements.

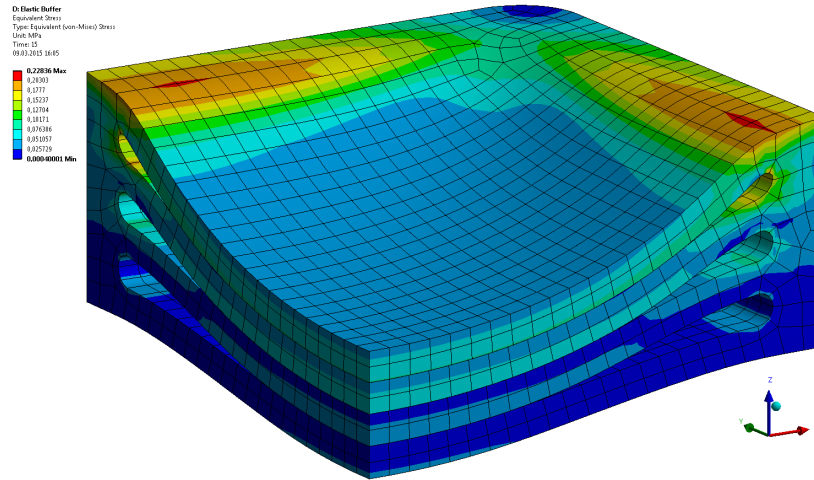


Figure 26: Equivalent von Mises stress obtained using ANSYS.

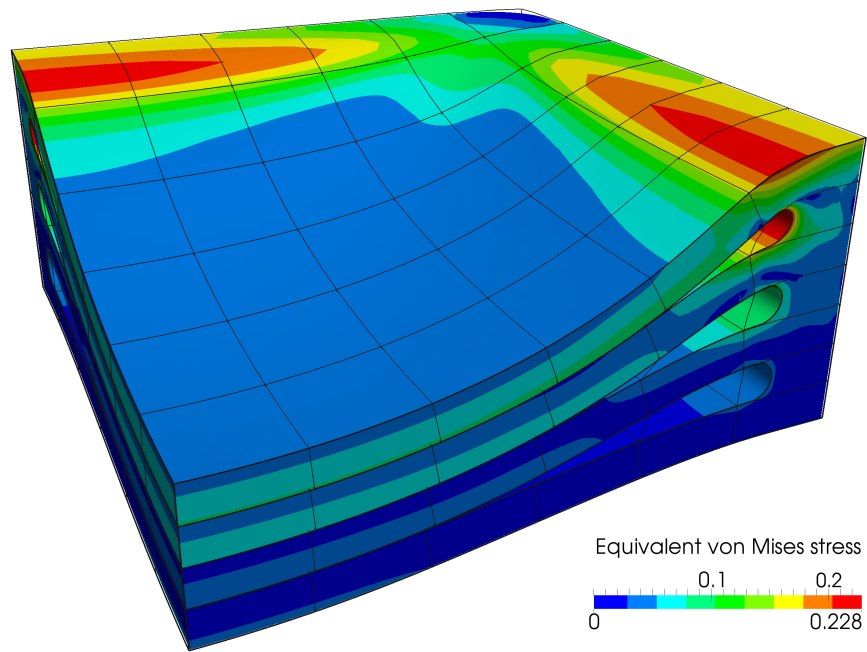


Figure 27: Equivalent von Mises stress obtained using the contact material ( $p = 5$ ).

However, applying the same ansatz order in the contact and the physical domain imposes an additional and unnecessary numerical burden for the Newton-Raphson procedure, inhibiting a reduction of the error level to lower thresholds. These difficulties can be overcome by either choosing a lower penalization of the contact material or by deactivating higher-order modes in the contact domain only. As long as the contact interface is still resolved with high order shape functions, no reduction in accuracy was observed. It also lies in line with the usual implementation of hierarchical ansatz spaces and has the added advantage that it leads to less degrees of freedom.

Our formulation tracks the contact status at the integration points by evaluating the principal stretches. Hence, the influence of the number of integration points on the resulting minimum gap was investigated. The results showed that for discretizations involving large elements with strongly curved boundaries, penetrations can occur if not enough integration points are present in the contact domain. This is an effect, however, common for most contact formulations.

The utilization of a contact material can be classified as a kind of barrier method. These methods have the property that penetrations are avoided at all times. Unfortunately, they also leave small gaps where, ideally, the contact interfaces should touch. A parameter study served to assess the influence of the contact stiffness on the final gap. The results showed that final gaps can be reduced to very small magnitudes by choosing small values of contact stiffness. Moreover, the contact stiffness turned out to be the most influential parameter in comparison to the ansatz order and the number of integration points.

As shown by the numerical examples, the formulation proposed in this paper has the advantage that explicit geometric searches on the global and local level can be avoided. Applying high order finite elements allows structures to be discretized for a desired approximation accuracy with a much smaller number of degrees of freedom compared to the  $h$ -version of the FEM.

A possible extension to the proposed formulation is the incorporation of friction. This will call for a more sophisticated and most likely anisotropic material formulation. Another interesting research direction is the investigation of alternative material models that work robustly also in the case of interface penetrations.

## Acknowledgements

The financial support by the German Research Foundation (DFG) under grant number RA 624/15-2 is gratefully acknowledged.

## References

- [1] P. Wriggers, Computational contact mechanics, 2nd Edition, Springer, Berlin, New York, 2006.

- [2] T. A. Laursen, Computational contact and impact mechanics: fundamentals of modeling interfacial phenomena in nonlinear finite element analysis, Springer, Berlin, 2002.
- [3] A. Francavilla, O. C. Zienkiewicz, A note on numerical computation of elastic contact problems, *International Journal for Numerical Methods in Engineering* 9 (4) (1975) 913–924. doi:10.1002/nme.1620090410.
- [4] J. T. Oden, Exterior penalty methods for contact problems in elasticity, in: W. Wunderlich, Erwin Stein, Klaus Jürgen Bathe (Eds.), *Nonlinear Finite Element Analysis in Structural Mechanics*, Springer, Berlin Heidelberg, 1981, pp. 655–665.
- [5] N. Kikuchi, J. T. Oden, Contact problems in elasticity: a study of variational inequalities and finite element methods, SIAM, Philadelphia, 1988.
- [6] J. O. Hallquist, NIKE2D: an Implicit, Finite-deformation, Finite-element Code for Analyzing the Static and Dynamic Response of Two-dimensional Solids, Lawrence Livermore Laboratory, University of California, Berkeley, 1979.
- [7] P. Wriggers, T. Vu Van, E. Stein, Finite element formulation of large deformation impact-contact problems with friction, *Computers & Structures* 37 (3) (1990) 319–331. doi:10.1016/0045-7949(90)90324-U.
- [8] B. I. Wohlmuth, A comparison of dual lagrange multiplier spaces for mortar finite element discretizations, *ESAIM: Mathematical Modelling and Numerical Analysis* 36 (6) (2003) 995–1012. doi:10.1051/m2an:2003002.
- [9] B. I. Wohlmuth, Variationally consistent discretization schemes and numerical algorithms for contact problems, *Acta Numerica* 20 (2011) 569–734. doi:10.1017/S0962492911000079.
- [10] M. A. Puso, A 3d mortar method for solid mechanics, *International Journal for Numerical Methods in Engineering* 59 (3) (2004) 315–336. doi:10.1002/nme.865.
- [11] M. A. Puso, T. A. Laursen, A mortar segment-to-segment contact method for large deformation solid mechanics, *Computer Methods in Applied Mechanics and Engineering* 193 (6–8) (2004) 601–629. doi:10.1016/j.cma.2003.10.010.
- [12] K. A. Fischer, P. Wriggers, Frictionless 2d contact formulations for finite deformations based on the mortar method, *Computational Mechanics* 36 (3) (2005) 226–244. doi:10.1007/s00466-005-0660-y.
- [13] K. A. Fischer, P. Wriggers, Mortar based frictional contact formulation for higher order interpolations using the moving friction cone, *Computer Methods in Applied Mechanics and Engineering* 195 (37–40) (2006) 5020–5036. doi:10.1016/j.cma.2005.09.025.

- [14] A. Popp, M. W. Gee, W. A. Wall, A finite deformation mortar contact formulation using a primal-dual active set strategy, *International Journal for Numerical Methods in Engineering* 79 (11) (2009) 1354–1391. doi:10.1002/nme.2614.
- [15] A. Popp, A. Seitz, M. W. Gee, W. A. Wall, Improved robustness and consistency of 3d contact algorithms based on a dual mortar approach, *Computer Methods in Applied Mechanics and Engineering* 264 (2013) 67–80. doi:10.1016/j.cma.2013.05.008.
- [16] D. C. Franke, A. Düster, E. Rank, The p-version of the FEM for computational contact mechanics, *PAMM* 8 (1) (2008) 10271–10272. doi:10.1002/pamm.200810271.
- [17] A. Konyukhov, K. Schweizerhof, Incorporation of contact for high-order finite elements in covariant form, *Computer Methods in Applied Mechanics and Engineering* 198 (13-14) (2009) 1213–1223. doi:10.1016/j.cma.2008.04.023.
- [18] D. C. Franke, A. Düster, V. Nübel, E. Rank, A comparison of the h-, p-, hp-, and rp-version of the FEM for the solution of the 2d hertzian contact problem, *Computational Mechanics* 45 (5) (2010) 513–522. doi:10.1007/s00466-009-0464-6.
- [19] İ. Temizer, P. Wriggers, T. J. R. Hughes, Three-dimensional mortar-based frictional contact treatment in isogeometric analysis with NURBS, *Computer Methods in Applied Mechanics and Engineering* 209–212 (2012) 115–128. doi:10.1016/j.cma.2011.10.014.
- [20] M. E. Matzen, T. Cichosz, M. Bischoff, A point to segment contact formulation for isogeometric, NURBS based finite elements, *Computer Methods in Applied Mechanics and Engineering* 255 (2013) 27–39. doi:10.1016/j.cma.2012.11.011.
- [21] M. S. Bazaraa, *Nonlinear programming: theory and algorithms*, 3rd Edition, Wiley-Interscience, Hoboken, N.J, 2006.
- [22] D. G. Luenberger, *Linear and nonlinear programming*, 2nd Edition, Springer, New, NY, 2005.
- [23] G. Kloosterman, *Contact methods in finite element methods*, Doctoral thesis, Universiteit Twente, Enschede (2002).
- [24] P. Wriggers, G. Zavarise, A formulation for frictionless contact problems using a weak form introduced by Nitsche, *Computational Mechanics* 41 (3) (2008) 407–420. doi:10.1007/s00466-007-0196-4.
- [25] F. Chouly, P. Hild, Y. Renard, Symmetric and non-symmetric variants of Nitsche’s method for contact problems in elasticity: theory and numerical experiments, *Tech. Rep. hal-00776619* (2013).

- [26] R. H. Krause, B. I. Wohlmuth, A dirichlet–neumann type algorithm for contact problems with friction, *Computing and Visualization in Science* 5 (3) (2002) 139–148. doi:10.1007/s00791-002-0096-2.
- [27] E. Oñate, S. R. Idelsohn, M. A. Celigueta, R. Rossi, Advances in the particle finite element method for the analysis of fluid–multibody interaction and bed erosion in free surface flows, *Computer Methods in Applied Mechanics and Engineering* 197 (19-20) (2008) 1777–1800. doi:10.1016/j.cma.2007.06.005.
- [28] J. Oliver, S. Hartmann, J. Cante, R. Weyler, J. Hernández, A contact domain method for large deformation frictional contact problems. Part 1: Theoretical basis, *Computer Methods in Applied Mechanics and Engineering* 198 (33-36) (2009) 2591–2606. doi:10.1016/j.cma.2009.03.006.
- [29] S. Hartmann, J. Oliver, R. Weyler, J. Cante, J. Hernández, A contact domain method for large deformation frictional contact problems. Part 2: Numerical aspects, *Computer Methods in Applied Mechanics and Engineering* 198 (33-36) (2009) 2607–2631. doi:10.1016/j.cma.2009.03.009.
- [30] P. Wriggers, J. Schröder, A. Schwarz, A finite element method for contact using a third medium, *Computational Mechanics* 52 (4) (2013) 837–847. doi:10.1007/s00466-013-0848-5.
- [31] J. Parvizian, A. Düster, E. Rank, Finite cell method, *Computational Mechanics* 41 (1) (2007) 121–133. doi:10.1007/s00466-007-0173-y.
- [32] A. Düster, J. Parvizian, Z. Yang, E. Rank, The finite cell method for three-dimensional problems of solid mechanics, *Computer Methods in Applied Mechanics and Engineering* 197 (45–48) (2008) 3768–3782. doi:10.1016/j.cma.2008.02.036.
- [33] P. Wriggers, *Nonlinear finite element methods*, Springer, Berlin, 2008.
- [34] I. Babuska, Manil Suri, The p- and h-p versions of the finite element method, an overview, *Computer Methods in Applied Mechanics and Engineering* 80 (1-3) (1990) 5–26. doi:10.1016/0045-7825(90)90011-A.
- [35] I. Babuška, M. Suri, The p and h-p versions of the finite element method, basic principles and properties, *SIAM Review* 36 (4) (1994) 578–632. doi:10.1137/1036141.
- [36] G. A. Holzapfel, *Nonlinear solid mechanics: a continuum approach for engineering*, Wiley, Chichester; New York, 2000.
- [37] J. Bonet, R. D. Wood, *Nonlinear Continuum Mechanics For Finite Element Analysis*, 2nd Edition, Cambridge University Press, Cambridge, 2008.
- [38] T. J. R. Hughes, *The finite element method: linear static and dynamic finite element analysis*, Dover Publications, Mineola, NY, 2000.

- [39] B. A. Szabó, A. Düster, E. Rank, The p-version of the finite element method, in: E. Stein (Ed.), *Encyclopedia of Computational mechanics*, John Wiley & Sons, Ltd, Chichester, West Sussex, 2004.
- [40] E. Rank, A. Düster, V. Nübel, K. Preusch, O. Bruhns, High order finite elements for shells, *Computer Methods in Applied Mechanics and Engineering* 194 (21-24) (2005) 2494–2512. doi:10.1016/j.cma.2004.07.042.
- [41] D. Schillinger, E. Rank, An unfitted hp-adaptive finite element method based on hierarchical b-splines for interface problems of complex geometry, *Computer Methods in Applied Mechanics and Engineering* 200 (47-48) (2011) 3358–3380. doi:10.1016/j.cma.2011.08.002.
- [42] M. Ruess, D. Schillinger, Y. Bazilevs, V. Varduhn, E. Rank, Weakly enforced essential boundary conditions for NURBS-embedded and trimmed NURBS geometries on the basis of the finite cell method, *International Journal for Numerical Methods in Engineering* 95 (10) (2013) 811–846. doi:10.1002/nme.4522.
- [43] S. Duczek, M. Joulaian, A. Düster, U. Gabbert, Simulation of lamb waves using the spectral cell method, 2013, pp. 86951U–86951U–11. doi:10.1117/12.2009983.
- [44] S. Duczek, M. Joulaian, A. Düster, U. Gabbert, Numerical analysis of lamb waves using the finite and spectral cell methods, *International Journal for Numerical Methods in Engineering* 99 (1) (2014) 26–53. doi:10.1002/nme.4663.
- [45] M. Dauge, A. Düster, E. Rank, Theoretical and numerical investigation of the finite cell method, Tech. Rep. hal-00850602, version 2, Université de Rennes (2014).
- [46] D. Schillinger, M. Ruess, The finite cell method: A review in the context of higher-order structural analysis of CAD and image-based geometric models, *Archives of Computational Methods in Engineering* (2014) 1–65doi:10.1007/s11831-014-9115-y.
- [47] M. A. Crisfield, *Non-linear finite element analysis of solids and structures*, Wiley, New York, 1997.
- [48] ANSYS, Inc., ANSYS Release 14.0, Help System, Element Reference, 2011.
- [49] V. Nübel, A. Düster, E. Rank, An rp-adaptive finite element method for the deformation theory of plasticity, *Computational Mechanics* 39 (5) (2007) 557–574. doi:10.1007/s00466-006-0111-4.
- [50] D. Schillinger, A. Düster, E. Rank, The hp-d-adaptive finite cell method for geometrically nonlinear problems of solid mechanics, *International Journal for Numerical Methods in Engineering* 89 (9) (2012) 1171–1202. doi:10.1002/nme.3289.

- [51] N. Zander, T. Bog, S. Kollmannsberger, D. Schillinger, E. Rank, Multi-level hp-adaptivity: high-order mesh adaptivity without the difficulties of constraining hanging nodes, *Computational Mechanics* 55 (3) (2015) 499–517. doi:10.1007/s00466-014-1118-x.
- [52] H. Hertz, Ueber die Berührung fester elastischer Körper., *Journal für die reine und angewandte Mathematik* 92 (1882) 156–171, 00000.
- [53] W. Gordon, C. Hall, Transfinite element methods: blending-function interpolation over arbitrary curved element domains, *Numerische Mathematik* 21 (2) (1973) 109–129.
- [54] D. Franke, Investigation of mechanical contact problems with high-order finite element methods, *Doctoral thesis*, Technische Universität München (2011).